Online-Journals.org

iTDAF IETI Transactions on
Data Analysis and Forecasting

iTDAF | eISSN: 2959-0442 | Vol. 4 No. 2 (2026) | OPEN ACCESS

https://doi.org/10.3991/itdaf.v4i2.60397

PAPER

UAV-Based Multi-Sensor Fusion for Leaf Age Detection in Maize Inbred Line Population Seedlings

Yibo Wei[1], Dong Cai[2], Haoyu Wang[1], Xinyi Wang[1], Xiaohong Du[1], Jiangchuan Fan[1](✉)

[1]Beijing Academy of Agriculture and Forestry Sciences, Beijing, China

[2]NongXin Science & Technology (Tianjin) Co., Ltd., Tianjin, China

fanjc@nercita.org.cn

ABSTRACT

Accurate and rapid detection of maize seedling growth is critical in early breeding decision-making, smart management, and yield improvement. Traditional leaf age detection still relies heavily on labor-intensive and low-efficiency manual field surveys, underscoring the urgent need for high-throughput phenotyping. Integrating multisource sensor data from unmanned aerial vehicle (UAV) with measured information such as crop height can further enhance the estimation accuracy of crop phenotypic parameters. Accurate field plot segmentation is critical for field-scale phenotypic analysis. However, current approaches remain largely dependent on slow, manual segmentation. Automating this step would greatly reduce the workload of agronomists. This study used UAV RGB and multispectral imagery collected over maize inbred line population plots before the canopy closure stage to perform automatic plot segmentation on field orthophotos and combined measured plant height with relative flight dates to achieve high-throughput detection of leaf age during the maize seedling stage. First, this study proposed a maize plot automatic segmentation method based on orthophotos. Then, it extracted texture features, RGB, and multispectral vegetation indices of each plot. Combined with relative flight date and plant height, four datasets were constructed. Support vector regression (SVR), random forest regression (RFR), and automatic machine learning (AutoML) regression algorithms were used to build the leaf age detection model. The results showed that the orthomosaic from March 23 achieved the best plot-segmentation performance, with minimum intersection over union (IoU), mean IoU, and IoU standard deviation of 14.67%, 96.47%, and 8.65%, respectively. Incorporating relative flight dates and plant-height measurements improved model performance, and the AutoML demonstrated the greatest robustness, achieving a validation R^2 of up to 0.862 and an RMSE as low as 0.715. This study proposed a leaf age estimation method that offers practical technical support for field-based maize seedling assessment and reduces manual labor demands.

KEYWORDS

multi-source sensors, plot segmentation, automatic machine learning (AutoML), maize leaf age

Wei, Y., Cai, D., Wang, H., Wang, X., Du, X., Fan, J. (2026). UAV-Based Multi-Sensor Fusion for Leaf Age Detection in Maize Inbred Line Population Seedlings. *IETI Transactions on Data Analysis and Forecasting (iTDAF)*, 4(2), pp. 4–24. https://doi.org/10.3991/itdaf.v4i2.60397

Article submitted 2025-12-26. Revision uploaded 2026-04-01. Final acceptance 2026-04-01.

1 INTRODUCTION

Leaf age during the maize seedling stage is a critical indicator of crop developmental status and plays an essential role in agronomic management, breeding decision-making, and yield formation [1, 2]. Accurate characterization of leaf development dynamics enables a more comprehensive understanding of crop responses to environmental conditions and supports optimized management strategies [3]. In maize breeding programs, especially those involving inbred line populations, the ability to efficiently monitor leaf age at scale is particularly important, as large numbers of genotypes must be evaluated within limited field space.

Conventional leaf age assessment relies primarily on manual leaf counting and visual evaluation of leaf expansion. Although widely adopted, these approaches are labor-intensive, time-consuming, and subject to observer bias, making them unsuitable for high-throughput phenotyping [4, 5]. To address these limitations, early studies primarily developed leaf age estimation indices based on established leaf growth curves under controlled indoor environments [4, 6, 7]. Consequently, there is a need for robust methodologies capable of estimating leaf age under complex field conditions.

With the rapid advancement of computer vision techniques, extracting leaf-level features from images to estimate leaf age has gained considerable research attention [8–10]. RGB image-based methods have been widely investigated due to their low cost and high spatial resolution, enabling the extraction of canopy color and texture features related to leaf development. However, accurate leaf age estimation remains challenging due to the diversity in leaf morphology, posture, and appearance, as well as frequent inter-leaf overlap and occlusion [11]. Moreover, many existing studies have been validated on publicly available RGB datasets, which may not fully represent real-world field conditions characterized by variable illumination, complex soil backgrounds, and dense canopy structures. Therefore, reliable leaf age estimation under plot-scale conditions presents a significant persistent challenge in the field of high-throughput phenotyping.

Given the complexity of leaf age estimation, which is influenced by multiple interacting factors, the development of accurate methods that can effectively leverage high-dimensional data from multi-sensor systems is of particular importance. Y. Bai et al. (2023) combined unmanned aerial vehicle (UAV) RGB and multispectral imaging with XGBoost and GBDT to detect maize seedling leaf age at the individual plant level [1]. In addition, incorporating ground-measured variables—such as plant height, nutrient status, or phenological timing—has been reported to improve model performance by partially compensating for sensor-related uncertainties. For example, W. Zhai et al. (2023) improved maize AGB prediction by incorporating SPAD measurements [12], and Y. Liu et al. (2023) enhanced yield estimation by introducing a lodging index [13]. Despite these advances, many existing studies focus either on individual plant-level analysis or on large-area field-scale estimation, while the intermediate plot scale, which is particularly relevant for breeding trials, has received comparatively less attention.

Automatic plot segmentation from UAV orthophotos is a critical prerequisite for high-throughput, plot-level phenotyping. Field experiments often consist of hundreds to thousands of plots, and manual delineation of plot boundaries across multi-temporal datasets is both time-consuming and prone to inconsistency. Existing plot segmentation methods include traditional image processing techniques and deep learning-based approaches. Traditional methods are generally computationally efficient and do not require annotated datasets [14–16], but their performance may vary under different crop growth stages and field conditions. Deep learning (DL) approaches can achieve high segmentation accuracy [17]; however, they typically require large annotated datasets and substantial computational resources, which may limit their practicality for high-frequency monitoring tasks. Furthermore, although a number of studies have explored plot segmentation using UAV imagery, many methods are developed under relatively controlled conditions or specific growth stages, and their robustness under complex scenarios—such as high-resolution orthophotos with dense plot distributions and temporally varying, indistinct boundaries caused by canopy overlap—remains a challenge.

Despite these advances, several challenges remain in UAV-based leaf age detection. First, robust automatic plot segmentation methods that can adapt to varying growth stages and canopy structures are still limited. Second, the integration of multi-source UAV data with ground-measured variables has not been fully explored for leaf age estimation. Third, conventional machine learning approaches often rely on manual model selection and hyperparameter tuning, which may limit scalability and generalization when applied to heterogeneous datasets.

To address these challenges, this study proposes a UAV-based multi-sensor fusion framework for maize leaf age detection at the plot scale. Specifically, we (i) developed an automatic plot segmentation method based on orthophotos combined with mean-shift correction to improve segmentation performance across different growth stages; (ii) constructed multi-source datasets by integrating RGB features, multispectral vegetation indices, plant height, and temporal information; and (iii) employed automated machine learning (AutoML) alongside conventional regression models to improve model robustness and predictive performance. The proposed framework enables high-throughput, plot-level phenotyping and provides technical support for maize breeding and field management.

2 MATERIALS AND METHODS

2.1 Experimental area and data acquisition

The experiments were conducted at the Hainan Breeding Experimental Station of the Beijing Academy of Agriculture and Forestry Sciences, located in western Sanya, Hainan Province (109°11′E, 18°23′N). The maize materials used in this study were derived from an association mapping panel developed by Professor Jianbing Yan at Huazhong Agricultural University. This panel encompasses a wide range of germplasm representing temperate, tropical, and subtropical ecotypes, thus capturing substantial genetic diversity across the maize gene pool. A total of 520 inbred lines were sown in March 2023 in a rectangular field measuring 70 m × 52 m (3,640 m^2), which was divided into 520 individual plots. Each plot was arranged with a row spacing of 55 cm and an intra-row plant spacing of 25 cm, comprising 20 plants (5 rows × 4 plants per row). Three seeds were sown per planting hill. Inter-plot spacing was maintained at 120 cm. For phenotyping purposes, a subset of plots was assigned an adjusted intra-row spacing of 60–80 cm to facilitate sampling. The overall planting density was approximately 6 plants per square meter. Starting from March 26, leaf age and plant height were measured every two days in 260 randomly selected plots, with three consecutive plants per plot monitored throughout the observation period. The geographical location of the experimental site and the spatial arrangement of plots are shown in Figure 1.

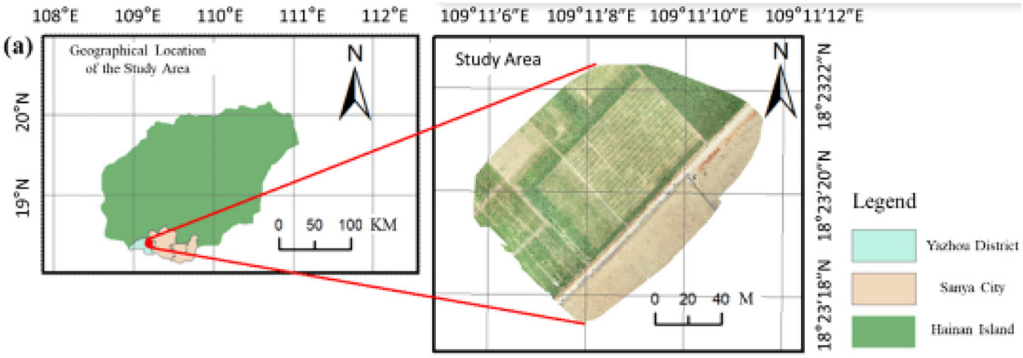

(a) Geographic location of the experimental site in Sanya, Hainan Province, China

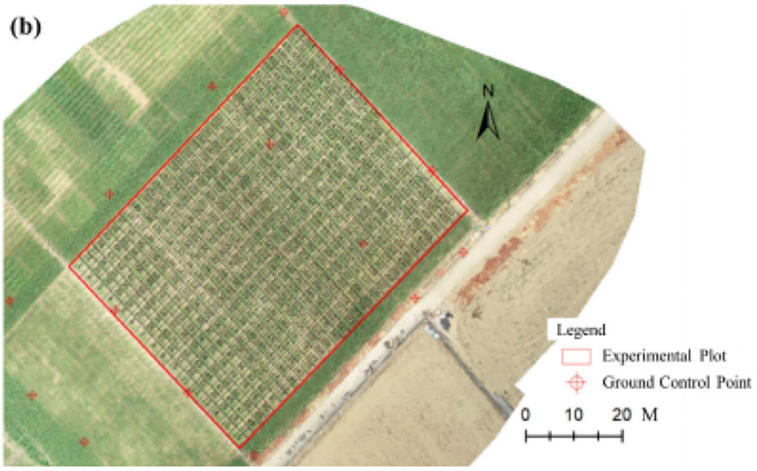

(b) Spatial distribution of plots in the experimental field

Fig. 1. Overview of the research area

The UAV-based remote-sensing dataset, comprising RGB and multispectral imagery, was acquired using a DJI Matrice 300 RTK (M300 RTK) platform. The UAV was equipped with a Sony 5100 RGB camera and a MicaSense Altum PT multispectral sensor, with flight settings of 60% forward overlap and 60% side overlap. RGB images had a spatial resolution of 5472 × 3648 pixels and were stored in JPG format. The MicaSense Altum PT sensor contained five narrow spectral bands and one long-wave infrared (LWIR) band, with central wavelengths of 475 nm (blue), 560 nm (green), 668 nm (red), 717 nm (red edge), and 840 nm (near-infrared), and a thermal band covering 7.5–13.5 μm. Multispectral images had a spatial resolution of 2064 × 1544 pixels and were stored in TIFF format. The UAV platform and onboard sensors used in this study are illustrated in Figure 2. UAV-acquired RGB and multispectral images collected on April 1, 7, 9, 13, and 15, 2023, were used for subsequent analyses. Maize leaf age was determined based on manual leaf counting and assessment of leaf expansion, while plant height was measured with a tape measure from the base of the stem to the apical meristem. Plot-level averages of leaf age and plant height were calculated based on three representative plants per plot.

a) DJI Matrice 300 RTK drone.

b) Sony 5100 RGB camera.

c) MicaSense Altum PT multispectral sensor.

Fig. 2. UAV platform and onboard sensors

2.2 Data processing methods

The data processing workflow in this study comprised UAV image processing, plot-level segmentation, feature extraction, and the development of a leaf age detection model. The overall technical pipeline is illustrated in Figure 3.

Raw RGB and multispectral images were processed using Pix4Dmapper version 4.5.6 to generate orthomosaic images and digital surface models (DSMs). The projection coordinate system was set to WGS84 UTM Zone 49N, with a ground sampling distance of approximately 3 cm/pixel. A shapefile representing the field boundary was manually delineated based on the orthomosaic, and radiometric correction was applied to produce reflectance maps.

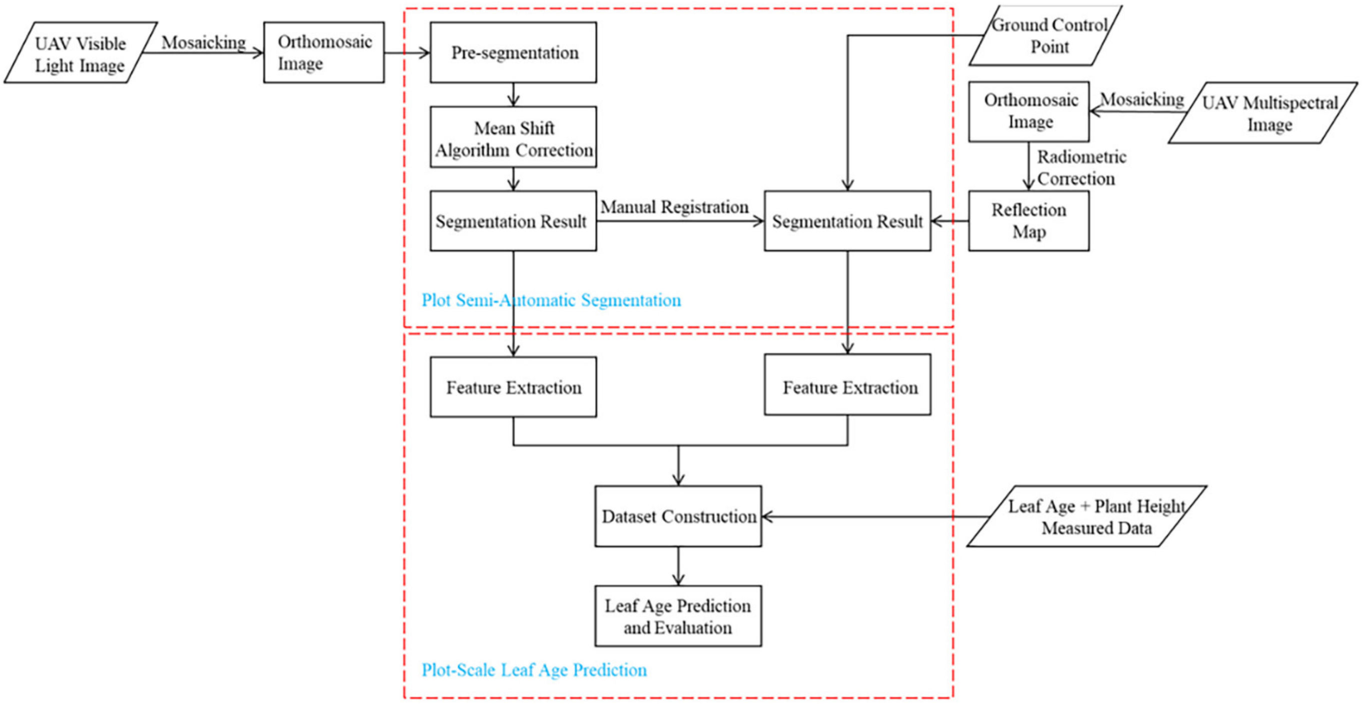

Fig. 3. Technical workflow of the data processing pipeline

2.3 Plot automatic segmentation method

Pre-segmented plots. The experimental field consisted of 16 rows and 33 columns of plots. The preprocessing steps prior to automatic plot segmentation were carried out as follows.

First, the Excess Green Vegetation Index (ExG) was computed to enhance vegetation features, using the formula:

$$ExG = 2g - r - b \tag{1}$$

where $r = \frac{R}{R+B+G}$, $g = \frac{G}{R+B+G}$, $b = \frac{B}{R+B+G}$.

Threshold segmentation was then applied to separate vegetated areas from the background.

Second, the orthomosaic was manually rotated to the horizontal orientation, and a quadrilateral was delineated to define the region of interest (ROI) covering the cultivated area, thereby excluding non-cultivated buffer strips (e.g., border rows). Based on the coordinates of vertices A, B, C, and D, the corresponding rectangular area was extracted from the orthomosaic and saved as a separate image file for further processing.

Finally, the vector segments $\overrightarrow{AB}$ and $\overrightarrow{DC}$ were each divided into 33 equal parts, and $\overrightarrow{AD}$ and $\overrightarrow{BC}$ into 16 equal parts. Corresponding division points along opposite edges were connected to form an orthogonal grid. The intersections of the grid lines—defined by the 33 equal divisions of $\overrightarrow{AB}$ and $\overrightarrow{DC}$, and the 16 equal divisions of $\overrightarrow{AD}$ and $\overrightarrow{BC}$—were used as the initial positions for automated plot segmentation.

Mean-shift algorithm correction. The plot regions derived from the intersection points of grid lines in Section 2.3.1 still exhibited positional offsets and did not fully encompass the vegetated areas within each plot. Because plot segmentation should aim to maximize the inclusion of vegetation while minimizing background, the vegetation mask obtained from the threshold segmentation in Section 2.3.1 was used as the reference for correction, and a Mean Shift algorithm was employed to refine the segmentation results. The procedure consisted of the following steps:

First, the initial positions generated in Section 2.3.1 were used as starting points, and an appropriate search window size (neighborhood radius) was determined for each point. Next, the centroid of vegetated pixels within the neighborhood was computed and used to update the position of the corresponding initial point. This process was iteratively repeated until the displacement of the centroids fell below a predefined convergence threshold.

The final corrected plot segmentation results—including vertex coordinates, width, height, and rotation angle of each plot—were saved in an Excel (.xlsx) file for subsequent analysis.

2.4 Alignment of RGB and multispectral imagery

In this study, manual registration was employed to align RGB and multispectral imagery, so that the vegetation mask derived from the RGB image and the plot segmentation results could be transformed into the multispectral imagery. The RGB and multispectral images were designated as the registration image (j) and the reference image (k), respectively, and six ground control points (GCPs) were manually identified across the field to serve as key correspondences.

The vegetation mask for the multispectral imagery was obtained by applying the Direct Linear Transform (DLT) to the vegetation mask derived from the RGB image, ensuring spatial alignment between the two datasets. To transform the plot segmentation results from the RGB image to the multispectral image, three geometric transformation parameters were computed: the scaling factors for width and height, the translation vector of plot vertices, and the rotation angle. Subsequently, each plot's position in the RGB image was translated, its width (w) and height (h) were scaled, and its orientation was rotated by an angle θ, as illustrated in Figure 4. The step-by-step procedure for transforming the plot segmentation results via manual registration is summarized in Table 1.

Table 1. Calculation of plot segmentation transformation parameters

Input: key points of images j and k, denoted as $k_{pi,j}$ and $k_{pi,k}$, respectively.
Output: θ, scale, $[u, v]^T$, H, i.e., rotation angle, scaling factor, translation vector, and transformation matrix.
1 $center_j$ $center_k$ ← Compute the centroid of the key points in images j and k: $\overline{kp_{i,j}}$ and $\overline{kp_{i,k}}$
2 for i = 1, 2, ……, NGCP do
3 $d_{i,j}$ and $d_{i,k}$ ← Compute the distances from the key points of images j and k to their respective centers, which are $\lVert kp_{i,j} - center_j \rVert$ and $\lVert kp_{i,k} - center_k \rVert$.
4. $\theta_{i,j}$ and $\theta_{i,k}$ ← Compute the angles between the key points of images j and k and their respective centers, specifically $\tan^{-1}\frac{(kp_{i,j} - center_j)[1]}{(kp_{i,j} - center_j)[0]}$ $\tan^{-1}\frac{(kp_{i,k} - center_k)[1]}{(kp_{i,k} - center_k)[0]}$
5 end
6 θ ← Compute the rotation angle, which is the average of the differences between $\theta_{i,j}$ and $\theta_{i,k}$, i.e., $\overline{(\theta_{i,j} - \theta_{i,k})}$
7 scale ← Compute the scale factor, which is the average of the ratios of $d_{i,j}$ and $d_{i,k}$, i.e., $\overline{d_{i,j}/d_{i,k}}$
8 $\begin{bmatrix} u_t \\ v_t \end{bmatrix}$ ← Compute the translation vector, which is $center_j^T - scale * \begin{bmatrix} \cos\theta & -\sin\theta \\ \sin\theta & \cos\theta \end{bmatrix} * center_k^T$
9 H ← Compute the transformation matrix, which is $\begin{bmatrix} scale*\cos\theta & -scale*\sin\theta & u_t \\ scale*\sin\theta & scale*\cos\theta & v_t \\ 0 & 0 & 1 \end{bmatrix}$

In analogy with the DLT, the coordinates (u, v) are transformed into (utrans, vtrans) via the homography matrix H, as shown in Equation 2.

$$u_{trans} = \frac{H[0,0]*u + H[0,1]*v + H[0,2]}{H[2,0]*u + H[2,1]*v + H[2,2]} \quad v_{trans} = \frac{H[1,0]*u + H[1,1]*v + H[1,2]}{H[2,0]*u + H[2,1]*v + H[2,2]} \tag{2}$$

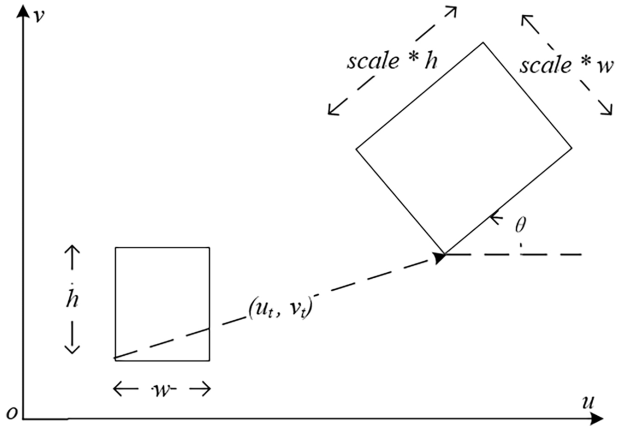

Fig. 4. Schematic diagram of the conversion of plot segmentation results

2.5 Extraction of texture and vegetation index features

The features extracted in this study comprised multispectral vegetation indices, as well as RGB vegetation index and texture features. Based on the vegetation and plot segmentation results from Section 2.4, the registered RGB orthophotos images and multispectral reflectance maps were cropped to the extent of each plot. For each plot, a feature image was generated, and the mean value of vegetated pixels within the plot was computed as the feature value. The extracted RGB features (vegetation indices and texture) and multispectral features (vegetation indices) are listed in Tables 3 and 4, respectively.

Table 2. Features selected from RGB images and their definitions

Feature	Definition	References
Normalized red band	$r = R/(R + G + B)$	[18]
Normalized green band	$g = G/(R + G + B)$	[18]
Normalized blue band	$b = B/(R + G + B)$	[18]
Excess Green	$ExG = 2g - r - b$	[18]
Excess Red	$ExR = 1.4r - g$	[19]
Excess Green minus excess Red	$ExGR = 3g - 2.4r - b$	[19]
Normalized Green-Red Difference Index	$NGRDI = (g - r)/(g + r)$	[19]
Red Green Blue Vegetation Index	$RGBVI = (g^2 - br)/(g^2 + br)$	[20]
Normalized Green-Blue Difference Index	$NGBDI = (g - b)/(g + b)$	[21]
Green-Red Ratio Index	$GRRI = g/r$	[21]
Green-Blue Ratio Index	$GBRI = g/b$	[21]
Blue-Red Ratio Index	$BRRI = b/r$	[21]
Color Index of Vegetation	$CIVE = 0.441r - 0.881g + 0.38b + 18.78745$	[21]
Mean	$ME = \sum_{i,j=0}^{N-1} i(P_{i,j})$	[22]
Variance	$VA = \sum_{i,j=0}^{N-1} iP_{i,j}(i - ME)^2$	[22]
Homogeneity	$HO = \sum_{i,j=0}^{N-1} \frac{P_{i,j}}{1 + (i - j)^2}$	[22]
Contrast	$CO = \sum_{i,j=0}^{N-1} P_{i,j}(i - j)^2$	[22]
Dissimilarity	$DI = \sum_{i,j=0}^{N-1} P_{i,j}\lvert i - j\rvert$	[22]
ASM	$ASM = \sqrt{\sum_{i,j=0}^{N-1} P_{i,j}^2}$	[22]
Second Moment	$SE = \sum_{i,j=0}^{N-1} P_{i,j}^2$	[22]
Correlation	$COR = \sum_{i,j=0}^{N-1} P_{i,j} \frac{(i - \mu_i)(j - \mu_j)}{\sqrt{\sigma_i^2 \sigma_j^2}}$	[22]

Note: R, G, and B denote the grayscale values of the red, green, and blue bands of the visible-light images. σ_i and σ_j represent the standard deviations of $P(i,\cdot,r,\theta)$ and $P(\cdot,j,r,\theta)$, respectively, while μ_i and μ_j denote the means of $P(i,\cdot,r,\theta)$ and $P(\cdot,j,r,\theta)$.

Table 3. Vegetation index selected from multispectral imagery and its definition

Vegetation Index	Definition	References
Blue bands	R_{blue}	–
Green bands	R_{green}	–
Red bands	R_{red}	–
NIR bands	R_{nir}	–
Red Edge bands	$R_{red\ edge}$	–
Difference Vegetation Index	$DVI = R_{nir} - R_{red}$	[1]
Enhanced Vegetation Index	$EVI = 2.5 \times \frac{R_{nir} - R_{red}}{R_{nir} + 6R_{red} - 7.5R_{blue} + 1}$	[12]
Excess Green Vegetation Index	$ExG = 2R_{green} - R_{red} - R_{blue}$	[19]
Excess Green Minus Excess Red Index	$ExGR = 3R_{green} - 2.4R_{red} - R_{blue}$	[19]
Green Difference Vegetation	$GDVI = R_{nir} - R_{green}$	–
Green Normalized Difference Vegetation	$GNDVI = \frac{R_{nir} - R_{green}}{R_{nir} + R_{green}}$	[12]
Modified Soil Adjusted Vegetation Index	$MSAVI = (1 + L)\frac{R_{nir} - R_{red}}{R_{nir} + R_{red} + L}(L = 0.1)$	[23]
Modified Soil Adjusted Vegetation Index2	$MSAVI2 = R_{nir} + 0.5 - \frac{\sqrt{(2R_{nir} + 1)^2 - 8(R_{nir} - R_{red})}}{2}$	[23]
Modified Simple Ratio	$MSR = \frac{R_{nir} - R_{red} - 1}{\sqrt{R_{nir} + R_{red}} + 1}$	[23]
Normalized Difference Red Edge Index	$NDRE = \frac{R_{nir} - R_{red\ edge}}{R_{nir} + R_{red\ edge}}$	[24]
Normalized Difference Vegetation Index	$NDVI = \frac{R_{nir} - R_{red}}{R_{nir} + R_{red}}$	[24]
Ratio Between NIR and Red Bands	$NIR/R = \frac{R_{nir}}{R_{red}}$	[12]
Simplified Canopy Chlorophyll Content Index	$SCCCI = \frac{R_{nir} - R_{blue}}{R_{nir} - R_{red}}$	[24]
Structure-Insensitive Pigment Index	$SIPI = \frac{R_{nir} - R_{blue}}{R_{nir} + R_{red}}$	[23]
Chlorophyll Index Green	$CIG = \frac{R_{nir}}{R_{green}} - 1$	–
Chlorophyll Index Red Edge	$CIRE = \frac{R_{nir}}{R_{red\ edge}} - 1$	–
Difference of Atmospherically Resistant Vegetation Index	$DATT = \frac{R_{nir} - R_{red\ edge}}{R_{nir} - R_{red}}$	–
Greenness and Redness Atmospherically Stable Vegetation Index	$GOSAVI = (1 + L)\frac{R_{nir} - R_{green}}{R_{nir} + R_{green} + L}(L = 0.16)$	–

Note: R_{blue}, R_{green}, R_{red}, R_{nir}, and $R_{red\ edge}$ denote the reflectance of the blue, green, red, near-infrared, and red-edge bands in the multispectral reflectance images, respectively.

2.6 Construction of a leaf age detection model

In this study, leaf age detection models were constructed using three machine learning algorithms: Support vector regression (SVR), random forest regression (RFR), and AutoML. The dataset was divided into training and testing sets at a 4:1 ratio.

The SVR and RFR algorithms were implemented using the scikit-learn library. RFR is an ensemble learning method that constructs multiple decision trees and aggregates their predictions by averaging, thereby improving prediction accuracy and stability. Owing to its robustness and low susceptibility to overfitting, RFR was configured with 20 trees in this study.

The AutoML algorithm employed in this study was implemented via the H2O platform. It automatically builds a diverse set of candidate models—including gradient boosting machines (GBM), generalized linear models (GLM), distributed random forests (DRF), deep learning (DL), and stacked ensembles—by performing hyperparameter optimization to maximize performance and evaluates them on a validation set to select the best-performing model. In contrast, conventional machine learning approaches typically require manual model selection and parameter tuning. By leveraging a high degree of automation, AutoML lowers the barrier to entry for machine learning applications and also provides built-in model interpretability. In this study, 5-fold cross-validation and 20 base models were employed for the AutoML pipeline.

2.7 Evaluation indicators

Evaluation indicators for the leaf age detection model. In this study, the performance of the leaf age detection model was evaluated using the coefficient of determination (R^2), root mean squared error (*RMSE*), and relative root mean squared error (*rRMSE*), as defined in Equations 3, 4, and 5. Here, $\hat{y}_i$ denotes the predicted value, y_i represents the observed value, y_i is the mean of the observed values, and n is the total number of samples. R^2 quantifies the coefficient of determination between the predicted and observed values, with higher R^2 indicating better model fit. Lower *RMSE* and *rRMSE* values correspond to stronger predictive performance. represents the residual between the predicted and observed values, as defined in Equation 6.

$$R^2 = 1 - \frac{\sum_{i=1}^{n} (\hat{y}_i - y_i)^2}{\sum_{i=1}^{n} (y_i - \bar{y})^2} \tag{3}$$

$$RMSE = \sqrt{\frac{1}{n} \sum_{i=1}^{n} (\hat{y}_i - y_i)^2} \tag{4}$$

$$rRMSE = \frac{RMSE}{\bar{y}_i} \times 100\% \tag{5}$$

$$error\_y_i = \hat{y}_i - y_i \tag{6}$$

Evaluation indicators for automatic plot segmentation. The mean Intersection over Union (IoU) was employed in this study to evaluate the results of plot segmentation corrected using the mean-shift algorithm [15]. The automated segmentation from Section 2.3 was compared with manually delineated plots, and IoU was calculated, as shown in Figure 5 and Equation 7, where intersection and union denote the areas of the overlapping and combined regions, respectively.

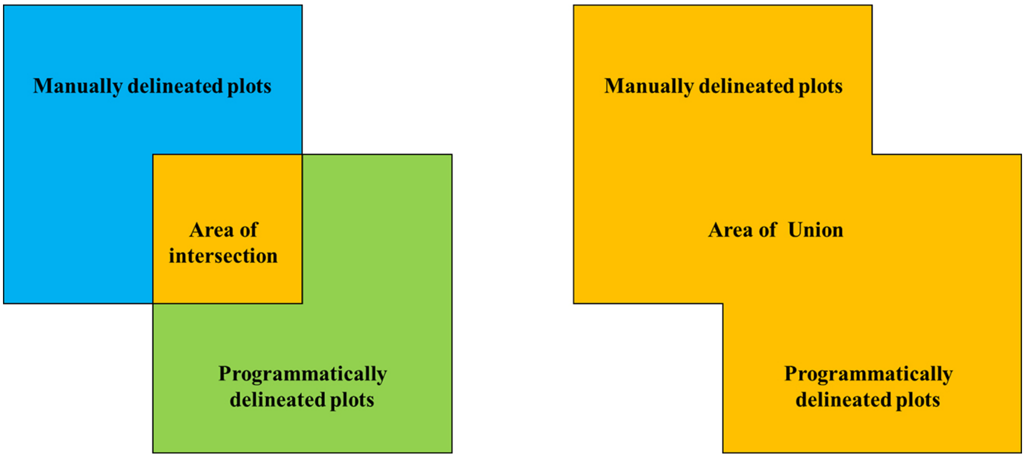

Fig. 5. Illustration of the IoU between manually and automatically segmented plots

3 RESULTS

3.1 Automatic plot segmentation results from time-series UAV orthophoto images

In this study, automatic plot segmentation was tested using orthomosaic images acquired on March 23, April 1, April 7, April 9, April 13, and April 15. The segmentation results are presented in Figure 6 and Table 4.

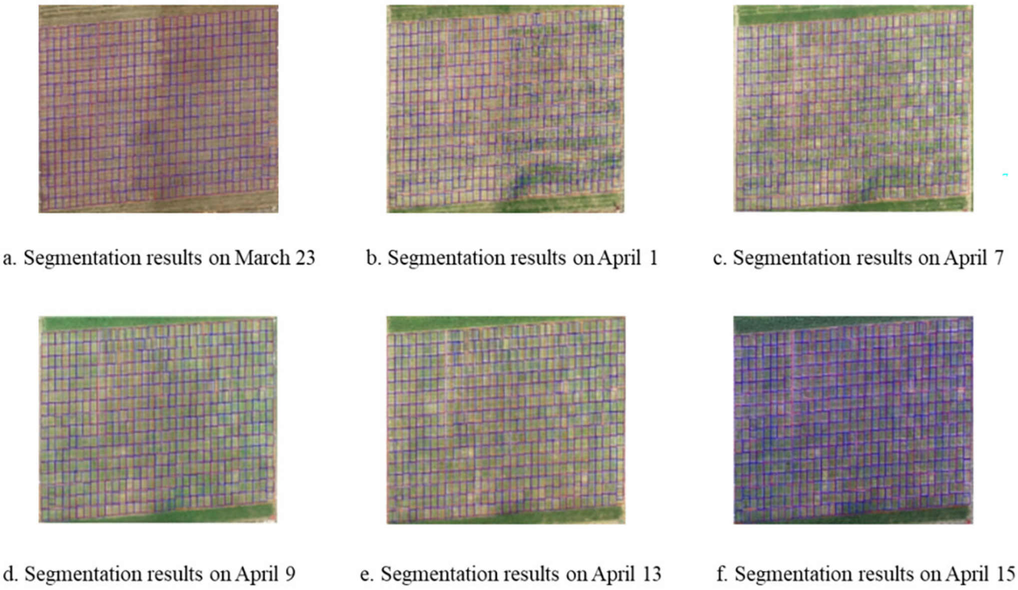
a. Segmentation results on March 23
b. Segmentation results on April 1
c. Segmentation results on April 7
d. Segmentation results on April 9
e. Segmentation results on April 13
f. Segmentation results on April 15

Fig. 6. All date segmentation results

The results indicate that the plot segmentation conducted on March 23 yielded the highest mean IoU and the lowest standard deviation, corresponding to the best segmentation performance. Segmentation results for certain dates were of lower quality, which can be attributed to three characteristics of the orthomosaic images. (1) At certain growth stages, maize leaves from different plots overlapped, interfering with the determination of plot boundaries; this phenomenon was observed on all dates except March 23. (2) Due to the limited resolution of the orthomosaic images, weeds could not be reliably distinguished from maize plants, resulting in weeds growing along plot boundaries being incorporated into the segmented plots by the Mean Shift algorithm, as seen on April 1 and April 7. (3) When maize seedlings were overly sparsely distributed, the Mean Shift algorithm tended to incorporate crops from neighboring plots during iteration, an effect that was evident in the last column of plots across all six acquisition dates.

Table 4. Statistical results of intersection and union ratios for different orthoimages

Date	Statistical Results for Intersection Ratio			
	Max	Min	Mean	SD
March 23	100%	14.67%	96.47%	8.65%
April 1	100%	32.17%	86.60%	17.12%
April 7	100%	31.93%	93.56%	13.49%
April 9	100%	9.29%	91.67%	14.84%
April 13	100%	18.19%	90.55%	13.89%
April 15	100%	4.77%	95.95%	14.00%

In this study, two software tools were developed based on the PyQt5 and PyQtGraph platforms. The first software was designed for non-specialists to perform automatic plot segmentation, and a semi-automatic numbering function was also implemented. The plot segmentation result for March 23 is shown in Figure 7a. The second software was developed for manual registration of orthomosaic images acquired on different dates, enabling transformation of the March 23 orthomosaic into the image coordinate system of the April 1 orthomosaic, as illustrated in Figure 7b. In Figure 7b, the registration error is given by Equations 8 and 9, where u_{ref}, v_{ref} represent the pixel coordinates of the reference image, $l_{u,i}$ and $l_{v,i}$ denote the registration errors in the u-axis and v-axis directions, and error i indicates the magnitude of the error.

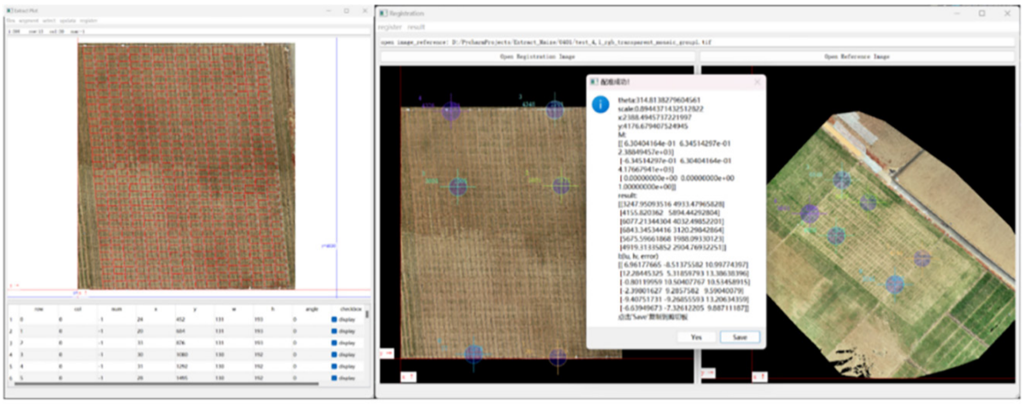

```
theta:314.8138279604561
scale:0.8944371432512822
x:2388.4945737221997
y:4176.679407524945
M:
[[ 6.30404164e-01  6.34514297e-01
2.38849457e+03]
 [-6.34514297e-01  6.30404164e-01
4.17667941e+03]
 [ 0.00000000e+00  0.00000000e+00
1.00000000e+00]]
result:
[[3247.95093516 4933.47965828]
 [4155.820362   5894.44292804]
 [6077.21344304 4032.49852201]
 [6843.34534416 3120.29842864]
 [5675.59661868 1988.09330123]
 [4919.31335852 2904.76932251]]
l:(lu, lv, error)
[[ 6.96177665 -8.51375582 10.99774397]
 [12.28445325  5.31859793 13.38638396]
 [-0.80119959 10.50407767 10.53458915]
 [-2.39001627  9.2857582   9.59040079]
 [-9.40751731 -9.26855593 13.20634359]
 [-6.63949673 -7.32612205  9.88711187]]
点击'Save'复制到剪切板
```

a. Community segmentation software interface b. Orthophoto registration software interface

Fig. 7. GUI of the two software programs

$$l_{u,i} = u_{trans} - u_{ref} \qquad l_{v,i} = v_{trans} - v_{ref} \tag{8}$$

$$error_i = \sqrt{l_{u,i}^2 + l_{v,i}^2} \tag{9}$$

3.2 Time-series variation analysis of important features

The temporal dynamics of the six key features—DATT, DVI, CIRE, Red, leaf age, and plant height—across five observation nodes (Days 1, 7, 9, 13, and 15) are illustrated in Figure 8. Overall, DATT, DVI, CIRE, and plant height exhibited significant positive trajectories that synchronized with the incremental progression of leaf age (Figure 8e), characterized by a rapid expansion phase between Day 1 and Day 7 followed by a steady maturation phase. Conversely, the Red (Figure 8d) reflectance demonstrated a consistent downward trend, reflecting the intensified light absorption driven by progressive chlorophyll accumulation as leaves matured. While DATT (Figure 8a) maintained high stability with concentrated distributions throughout the study period, indicators such as CIRE (Figure 8c) and plant height (Figure 8f) showed an expansion in interquartile ranges during later stages, suggesting an increase in phenotypic variability within the population over time.

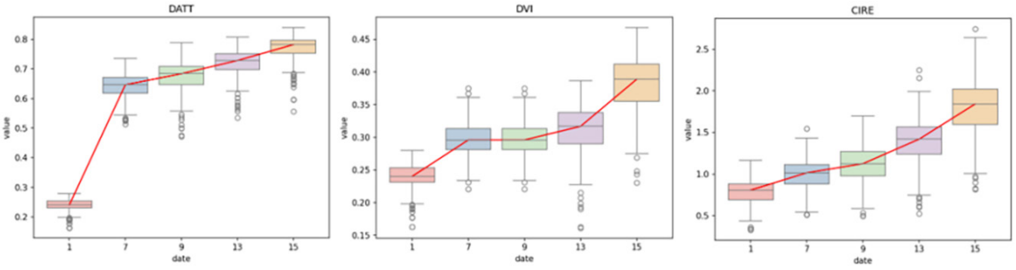

a. DATT b. DVI c. CIRE

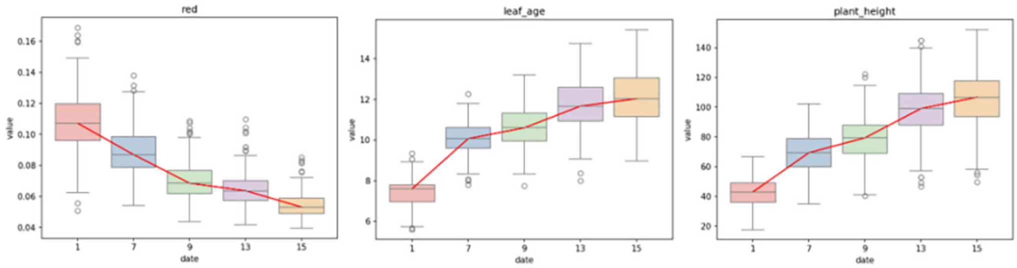

d. red e. leaf age f. plant height

Fig. 8. Temporal variations of partial features and measured values

3.3 Correlation coefficient matrix of features

In this study, we analyzed the correlations between the extracted RGB features, multispectral features, and the measured leaf age and visualized the correlation coefficients in a heatmap, as shown in Figure 9. The calculation of the correlation coefficient is given by Equation 10, where X and Y represent two input features, $\eta_{X,Y}$ represents the correlation coefficient between the two features,

X_i and Y_i denote the values of the X and Y features for each sample, X and Y are the means of X and Y across all samples, and σ_X and σ_Y are the corresponding standard deviations.

The Pearson correlation matrix (Figure 9a) illustrates the quantitative relationship between the extracted multispectral features and the measured leaf age. Leaf age exhibited strong positive correlations with several vegetation indices, most notably GNDVI (r = 0.82), CIG (r = 0.79), SIPI (r = 0.75), NDRE (r = 0.74), and CIRE (r = 0.73), indicating that these indicators are highly sensitive to the physiological maturation of the crop. In contrast, the visible bands (Blue, Green, and Red) and DVI showed significant negative correlations (|r| ≥ 0.72), which is consistent with the increased pigment absorption and spectral shifts observed during the leaf development process.

The correlation matrix between RGB-derived features and leaf age (Figure 9b) reveals moderate to strong associations, though the coefficients are generally lower than those observed for multispectral indices. Among the color-based indicators, NGBDI (r = 0.59) and GBRI (r = 0.57) exhibited the highest positive correlations with leaf age, while the blue band (r = –0.61) and BRRI (r = –0.58) showed the most significant negative correlations, reflecting the shift in pigment-driven color properties during maturation. Regarding textural features, dissimilarity (r = –0.54) and contrast (r = –0.60) demonstrated moderate negative trends, whereas energy (r = 0.49) was positively correlated with leaf age, suggesting a progression toward increased surface uniformity and reduced structural complexity as the leaves develop.

$$\eta_{X,Y} = \frac{\sum_{i=1}^{n}(X_i - \bar{X})(Y_i - \bar{Y})}{\sigma_X \cdot \sigma_Y} \tag{10}$$

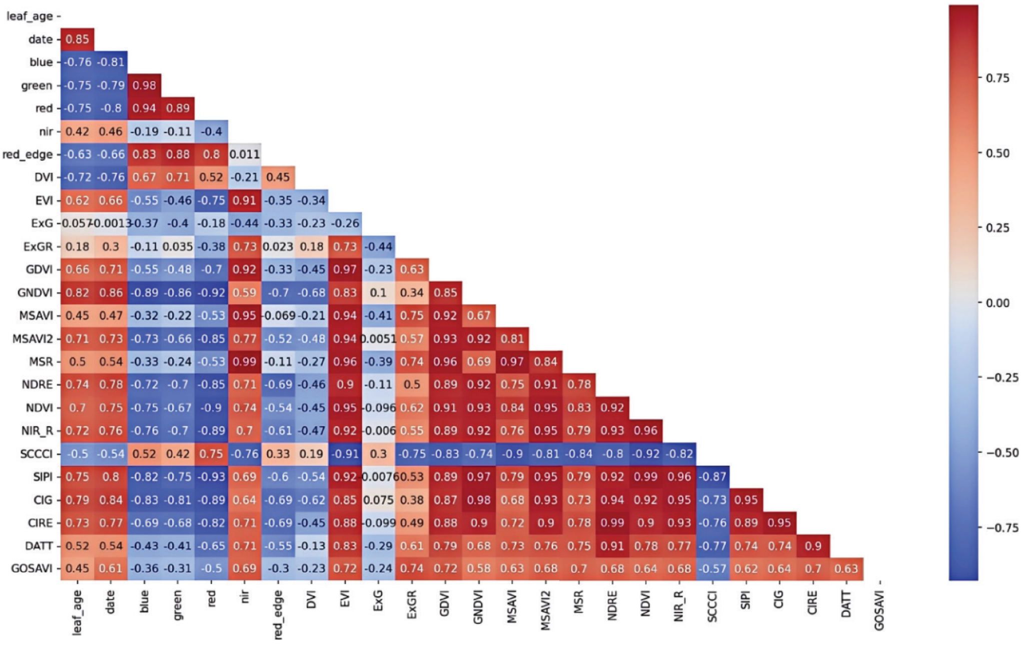

	leaf_age	date	blue	green	red	nir	red_edge	DVI	EVI	ExG	ExGR	GDVI	GNDVI	MSAVI	MSAVI2	MSR	NDRE	NDVI	NIR_R	SCCCI	SIPI	CIG	CIRE	DATT	GOSAVI
leaf_age																									
date	0.85																								
blue	-0.76	-0.81																							
green	-0.75	-0.79	0.98																						
red	-0.75	-0.8	0.94	0.89																					
nir	0.42	0.46	-0.19	-0.11	-0.4																				
red_edge	-0.63	-0.66	0.83	0.88	0.8	0.011																			
DVI	-0.72	-0.76	0.67	0.71	0.52	-0.21	0.45																		
EVI	0.62	0.66	-0.55	-0.46	-0.75	0.91	-0.35	-0.34																	
ExG	-0.057	-0.0013	-0.37	-0.4	-0.18	-0.44	-0.33	-0.23	-0.26																
ExGR	0.18	0.3	-0.11	0.035	-0.38	0.73	0.023	0.18	0.73	-0.44															
GDVI	0.66	0.71	-0.55	-0.48	-0.7	0.92	-0.33	-0.45	0.97	-0.23	0.63														
GNDVI	0.82	0.86	-0.89	-0.86	-0.92	0.59	-0.7	-0.68	0.83	0.1	0.34	0.85													
MSAVI	0.45	0.47	-0.32	-0.22	-0.53	0.95	-0.069	-0.21	0.94	-0.41	0.75	0.92	0.67												
MSAVI2	0.71	0.73	-0.73	-0.66	-0.85	0.77	-0.52	-0.48	0.94	0.0051	0.57	0.93	0.92	0.81											
MSR	0.5	0.54	-0.33	-0.24	-0.53	0.99	-0.11	-0.27	0.96	-0.39	0.74	0.96	0.69	0.97	0.84										
NDRE	0.74	0.78	-0.72	-0.7	-0.85	0.71	-0.69	-0.46	0.9	-0.11	0.5	0.89	0.92	0.75	0.91	0.78									
NDVI	0.7	0.75	-0.75	-0.67	-0.9	0.74	-0.54	-0.45	0.95	-0.096	0.62	0.91	0.93	0.84	0.95	0.83	0.92								
NIR_R	0.72	0.76	-0.76	-0.7	-0.89	0.7	-0.61	-0.47	0.92	-0.006	0.55	0.89	0.92	0.76	0.95	0.79	0.93	0.96							
SCCCI	-0.5	-0.54	0.52	0.42	0.75	-0.76	0.33	0.19	-0.91	0.3	-0.75	-0.83	-0.74	-0.9	-0.81	-0.84	-0.8	-0.92	-0.82						
SIPI	0.75	0.8	-0.82	-0.75	-0.93	0.69	-0.6	-0.54	0.92	-0.0076	0.53	0.89	0.97	0.79	0.95	0.79	0.92	0.99	0.96	-0.87					
CIG	0.79	0.84	-0.83	-0.81	-0.89	0.64	-0.69	-0.62	0.85	0.075	0.38	0.87	0.98	0.68	0.93	0.73	0.94	0.92	0.95	-0.73	0.95				
CIRE	0.73	0.77	-0.69	-0.68	-0.82	0.71	-0.69	-0.45	0.88	-0.099	0.49	0.88	0.9	0.72	0.9	0.78	0.99	0.9	0.93	-0.76	0.89	0.95			
DATT	0.52	0.54	-0.43	-0.41	-0.65	0.71	-0.55	-0.13	0.83	-0.29	0.61	0.79	0.68	0.73	0.76	0.75	0.91	0.78	0.77	-0.77	0.74	0.74	0.9		
GOSAVI	0.45	0.61	-0.36	-0.31	-0.5	0.69	-0.3	-0.23	0.72	-0.24	0.74	0.72	0.58	0.63	0.68	0.7	0.68	0.64	0.68	-0.57	0.62	0.64	0.7	0.63	

a) Correlation Coefficients: Multispectral Features vs. Measured Leaf Age

Fig. 9. *(Continued)*

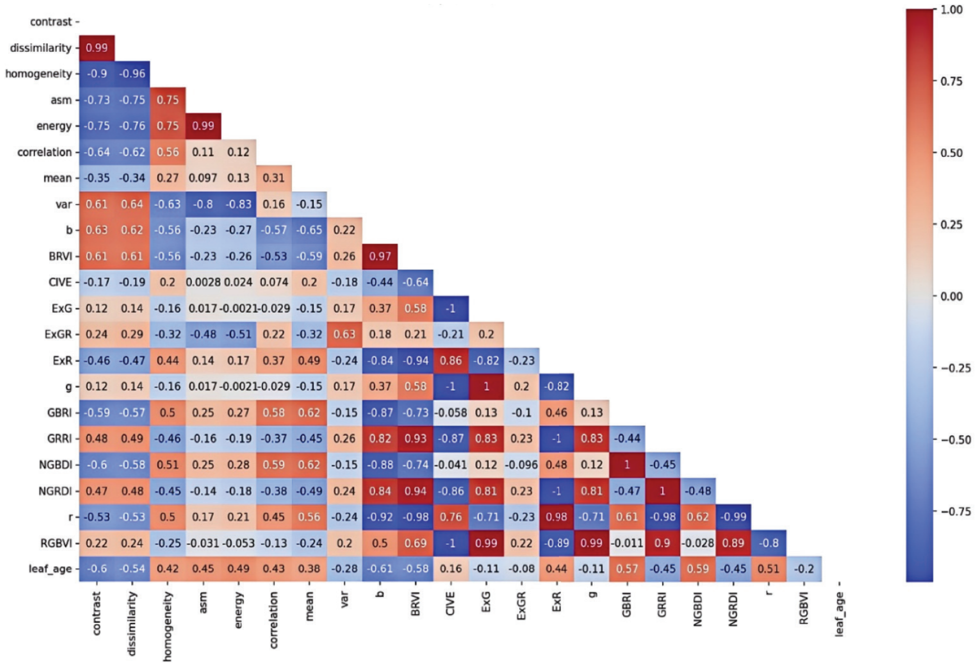

b) Correlation Coefficients: RGB Features vs. Measured Leaf Age

Fig. 9. Correlation between predictor variables and observed leaf age

After extracting features from multispectral and RGB images, datasets were constructed based on RGB, MS, and RGB + MS. For the RGB + MS dataset, features were selected from the RGB and MS sources on the basis of their Pearson correlation with the measured leaf age—specifically, those exhibiting a correlation coefficient $|r| > 0.5$ (i.e., $r > 0.5$ or $r < -0.5$). The RGB + MS + date + plant_height dataset was subsequently developed by augmenting the RGB + MS set with two additional predictors: the relative flight date (date) and plant height (plant_height). The variable date represents the number of days between March 31 and the acquisition date of the leaf age and plant height measurements, whereas plant_height corresponds to the mean of the three individual plant height measurements recorded for each plot, as detailed in Section 2.2. For all four datasets, the response variable was defined as the average plot-scale measured leaf age over a five-day period, yielding a total of 1,300 samples. Data was partitioned into training and testing subsets at a 4:1 ratio. Three regression approaches—SVR, RFR, and the h2o AutoML platform—were employed to develop leaf age prediction models. The features selected for the four datasets are listed in Table 5.

Table 5. Predictor variables selected within each dataset

Dataset	Total Features	Features Selected
RGB	21	r, g, b, ExG, ExR, ExGR, NGRDI, RGBVI, NGBDI, GRRI, GBRI, BRRI, CIVE, ME, VA, HO, CO, DI, ASM, SE, COR
MS	23	R_{blue}, R_{green}, R_{red}, R_{nir}, R_{red_edge}, DVI, EVI, ExG, ExGR, GDVI, GNDVI, MSAVI, MSAVI2, MSR, NDRE, NDVI, NIR/R, SCCCI, SIPI, CIG, CIRE, DATT, GOSAVI
RGB + MS	22	CO, DI, b, BRVI, GBRI, NGBDI, r, R_{blue}, R_{green}, R_{red}, R_{red_edge}, DVI, EVI, GDVI, GNDVI, MSAVI2, NDRE, NDVI, NIR/R, CIG, CIRE, DATT
RGB + MS + date + plant_height	24	CO, DI, b, BRVI, GBRI, NGBDI, r, R_{blue}, R_{green}, R_{red}, R_{red_edge}, DVI, EVI, GDVI, GNDVI, MSAVI2, NDRE, NDVI, NIR/R, CIG, CIRE, DATT, date, plant_height

3.4 Results of the leaf age detection model

The predictive performance of each dataset and model is summarized in Table 6. The AutoML algorithm achieved the best estimation performance on the RGB + MS + date + plant_height dataset, with a testing R^2 of 0.862, an RMSE of 0.715, and an rRMSE of 6.95%. Among the algorithms, RFR exhibited the best training performance ($R^2 = 0.981$), whereas AutoML exhibited superior performance on the corresponding test datasets. In the MS training dataset, the maximum difference in R^2 between RFR and AutoML was 0.106; however, the predicted results of the two algorithms were similar in the test dataset. The SVR algorithm exhibited lower R^2 values and higher RMSE and rRMSE than RFR and AutoML across both training and test datasets, indicating the poorest fitting capacity due to its inability to capture the complex relationships between features and leaf age. The RFR algorithm showed a greater discrepancy between training and test datasets, demonstrating lower robustness compared with AutoML. Across the four datasets, the RGB + MS + date + plant_height dataset exhibited the best training and estimation performance. This can be attributed to the presence of highly leaf-age-correlated texture features in the RGB dataset and highly leaf-age-correlated spectral features in the MS dataset, while leaf-age progression is also related to the flight date and plant height. Compared with the RGB + MS dataset, all three algorithms showed improved performance. Excluding features with low correlation to leaf age and incorporating the flight date and measured plant height contributed to enhanced estimation performance of maize seedling leaf age at the plot scale using the UAV platform.

Table 6. Model performance on different datasets

Dataset	Modeling Algorithm	Training			Testing		
		R^2	RMSE	rRMSE	R^2	RMSE	rRMSE
RGB	SVR	0.455	1.423	13.67%	0.556	1.244	12.05%
	RFR	0.959	0.385	3.69%	0.734	1.034	10.08%
	AutoML	0.877	0.670	6.43%	0.761	0.941	9.15%
MS	SVR	0.694	1.060	10.18%	0.677	1.094	10.59%
	RFR	0.964	0.361	3.49%	0.762	0.946	8.96%
	AutoML	0.858	0.722	6.93%	0.770	0.923	8.96%
RGB + MS	SVR	0.609	1.196	11.48%	0.610	1.207	11.72%
	RFR	0.962	0.369	3.55%	0.770	0.939	9.08%
	AutoML	0.872	0.685	6.58%	0.778	0.906	8.81%
RGB + MS + date + plant_height	SVR	0.739	0.977	9.37%	0.728	1.005	9.81%
	RFR	0.981	0.266	2.57%	0.817	0.810	7.63%
	AutoML	0.978	0.285	2.74%	0.862	0.715	6.95%

3.5 Distribution of prediction residuals for the leaf age detection model

For the datasets incorporating both visible-light and multispectral features, the error distributions of the three algorithms are presented in Figure 10. All three error distributions approximate a normal distribution, where μ and σ represent the mean and standard deviation of the normal distribution, respectively, and p denotes the result of a t-test comparing the model predictions with the observed values. The p-values for all three models exceeded 0.05, indicating no significant differences between the two datasets. The error distribution of the model constructed with the RFR algorithm exhibited the smallest standard deviation, whereas the model constructed with the SVR algorithm exhibited the largest standard deviation. After incorporating measured plant height and the relative flight date, the models constructed using the AutoML and SVR algorithms exhibited reductions in both the mean and standard deviation of errors (see Figure 11).

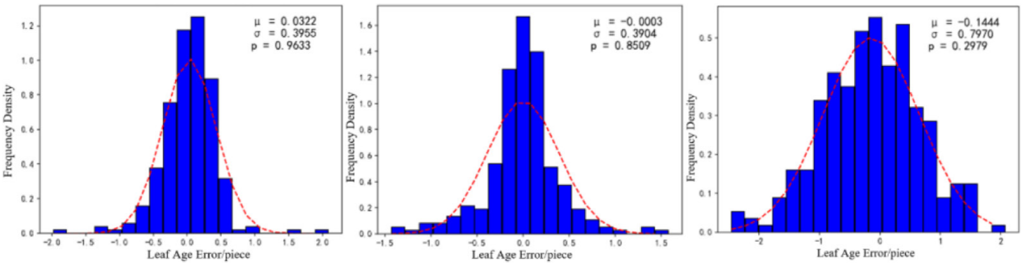

a) Residual distribution based on the AutoML algorithm. **b) Residual distribution based on the RFR algorithm.** **c) Residual distribution based on the SVR algorithm**

Fig. 10. Residual distribution of leaf age (Model without plant height and relative date features)

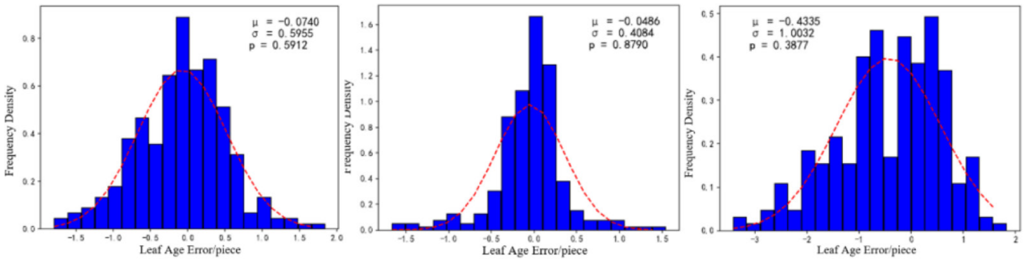

a) Residual distribution based on the AutoML algorithm. **b) Residual distribution based on the RFR algorithm.** **c) Residual distribution based on the SVR algorithm**

Fig. 11. Residual distribution of leaf age

4 DISCUSSION

4.1 Impact of plant height and relative flight date on the leaf age detection model

A comparison between the multi-sensor dataset (RGB + MS) and single-sensor datasets (RGB or MS) revealed that models based on RFR and AutoML achieved higher accuracy on the multi-sensor dataset, differing from the results reported by Y. Bai et al. [1]. High-resolution RGB imagery captures fine-scale texture variations, while multispectral indices reflect physiological and biochemical characteristics, jointly enhancing model performance. However, the stability of sensors may be influenced by various external environmental factors, such as crop growth conditions and soil characteristics [25]. Incorporating plant height and relative flight date significantly improved model performance by providing additional temporal and structural constraints.

4.2 Impact of regression algorithms on leaf age detection models

Among the evaluated algorithms, AutoML achieved superior generalization performance compared with SVR and RFR. Although RFR exhibited higher accuracy on the training set, its performance degraded on the test set, indicating potential overfitting. In contrast, AutoML maintained stable performance across datasets, benefiting from automated model selection and ensemble learning strategies. The improved robustness of AutoML can be attributed to its ability to integrate multiple base learners and optimize hyperparameters, reducing dependence on manual tuning. These results suggest that AutoML is a promising approach for handling high-dimensional, heterogeneous phenotyping datasets.

4.3 Contribution of automatic plot segmentation

The proposed plot segmentation method demonstrated adaptability across multiple growth stages, addressing challenges such as canopy overlap and sparse vegetation. Previous studies have often focused on specific growth stages or relatively stable conditions [16, 26], whereas this study evaluated segmentation performance using multi-temporal UAV data, enabling assessment under dynamically changing field environments. The best performance was achieved at early growth stages, when canopy structure was relatively simple and plot boundaries were distinct. As canopy complexity increased, segmentation accuracy declined, indicating that dynamic canopy conditions remain a key challenge for plot-level phenotyping. Additionally, this study implemented cross-sensor and cross-temporal plot transformation using manual registration, enabling consistent plot-level analysis across datasets. This strategy improves data usability but still requires manual intervention.

4.4 Limitations and future work

In this study, leaf age estimation was conducted at the plot scale using the average of three representative plants, which reflects the general growth status of each plot but may not fully capture within-plot variability. In addition, although the AutoML framework achieved superior predictive performance, the resulting ensemble models remain less interpretable, and the contribution of individual features has not been thoroughly quantified. Moreover, the proposed plot segmentation method was evaluated under relatively regular plot layouts, where plots were uniformly arranged and clearly structured. Such conditions may differ from more complex field scenarios with irregular plot shapes or heterogeneous spatial distributions, potentially limiting the general applicability of the method. Future work will therefore focus on extending the current framework to finer scales and more diverse conditions, including individual-plant-level phenotyping, enhanced model interpretability, and the development of more flexible segmentation approaches applicable to irregular field configurations and different cropping systems.

5 CONCLUSIONS

This study developed a UAV-based multi-sensor fusion framework for plot-level maize leaf age estimation by integrating RGB imagery, multispectral data, plant height, and temporal information. The results demonstrate that multi-source data fusion significantly improves prediction accuracy compared with single-sensor approaches.

Among the evaluated models, AutoML achieved the best overall performance and robustness, highlighting its effectiveness for high-dimensional phenotyping tasks. The incorporation of plant height and relative flight date further enhanced model accuracy by providing complementary structural and temporal information. In addition, the proposed automatic plot segmentation method enabled efficient extraction of plot-level features across multiple growth stages, although its performance was influenced by canopy complexity.

Overall, this study provides an effective and scalable solution for high-throughput plot-level phenotyping using UAV data. Future research will focus on improving model interpretability, extending segmentation methods to complex field conditions, and advancing toward individual-plant-level phenotyping.

6 ACKNOWLEDGEMENTS

This work was supported by the Beijing Academy of Agriculture and Forestry Sciences Reform and Development Project—Tianjin Institute of Smart Agriculture's Research and Demonstration of Plant Phenotyping and Intelligent Aquaculture Technology (Grant No. GGFZ20250410). Reform and Development Project of Beijing Academy of Agricultural and Forestry Sciences (Grant No. GGFZ20240101).

7 REFERENCES

[1] Y. Bai *et al.*, "Estimating leaf age of maize seedlings using UAV-based RGB and multispectral images," *Computers and Electronics in Agriculture*, vol. 215, p. 108349, 2023. https://doi.org/10.1016/j.compag.2023.108349

[2] A. Dobrescu, M. V. Giuffrida, and S. A. Tsaftaris, "Doing more with less: A multitask deep learning approach in plant phenotyping," *Frontiers in Plant Science*, vol. 11, p. 141, 2020. https://doi.org/10.3389/fpls.2020.00141

[3] M. A. Waqas *et al.*, "Thermal stresses in maize: Effects and management strategies," *Plants*, vol. 10, no. 2, p. 293, 2021. https://doi.org/10.3390/plants10020293

[4] R. O. Erickson and F. J. Michelini, "The plastochron index," *American Journal of Botany*, vol. 44, no. 4, pp. 297–305, 1957. https://doi.org/10.2307/2438380

[5] W. Su *et al.*, "Phenotyping of corn plants using Unmanned Aerial Vehicle (UAV) images," *Remote Sensing*, vol. 11, no. 17, p. 2021, 2019. https://doi.org/10.3390/rs11172021

[6] D. Swan, D. M. Brown, and M. C. Coligado, "Leaf emergence rates of corn (*ZEA MAYS* L.) as affected by temperature and photoperiod," *Agricultural Meteorology*, vol. 24, pp. 57–73, 1981. https://doi.org/10.1016/0002-1571(81)90033-9

[7] C.-C. Chen, H. Chen, and Y.-r. Chen, "A new method to measure leaf age: Leaf measuring-interval index," *American Journal of Botany*, vol. 96, no. 7, pp. 1313–1318, 2009. https://doi.org/10.3732/ajb.0800303

[8] J. Zhang *et al.*, "Rapeseed stand count estimation at leaf development stages with UAV imagery and convolutional neural networks," *Front. Plant Sci.*, vol. 11, p. 617, 2020. https://doi.org/10.3389/fpls.2020.00617

[9] S. Fei *et al.*, "UAV-based multi-sensor data fusion and machine learning algorithm for yield prediction in wheat," *Precision Agriculture*, vol. 24, no. 1, pp. 187–212, 2023. https://doi.org/10.1007/s11119-022-09938-8

[10] B. Biskup, H. Scharr, U. Schurr, and U. Rascher, “A stereo imaging system for measuring structural parameters of plant canopies,” *Plant, Cell & Environment*, vol. 30, no. 10, pp. 1299–1308, 2007. https://doi.org/10.1111/j.1365-3040.2007.01702.x

[11] H. Scharr *et al.*, “Leaf segmentation in plant phenotyping: A collation study,” *Machine Vision and Applications*, vol. 27, no. 4, pp. 585–606, 2016. https://doi.org/10.1007/s00138-015-0737-3

[12] W. Zhai *et al.*, “CatBoost algorithm for estimating maize above-ground biomass using unmanned aerial vehicle-based multi-source sensor data and SPAD values,” *Computers and Electronics in Agriculture*, vol. 214, p. 108306, 2023. https://doi.org/10.1016/j.compag.2023.108306

[13] Y. Liu *et al.*, “Evaluating how lodging affects maize yield estimation based on UAV observations,” *Frontiers in Plant Science*, vol. 13, p. 979103, 2022. https://doi.org/10.3389/fpls.2022.979103

[14] Z. Khan and S. J. Miklavcic, “An automatic field plot extraction method from aerial orthomosaic images,” *Frontiers in Plant Science*, vol. 10, p. 683, 2019. https://doi.org/10.3389/fpls.2019.00683

[15] L. Tresch *et al.*, “Easy MPE: Extraction of quality microplot images for UAV-based high-throughput field phenotyping,” *Plant Phenomics*, vol. 2019, p. 2591849, 2019. https://doi.org/10.34133/2019/2591849

[16] T. Ha, H. Duddu, A. Vandenberg, and S. Shirtliffe, “A semi-automatic workflow for plot boundary extraction of irregularly sized and spaced field plots from UAV imagery,” *The Plant Phenome Journal*, vol. 5, no. 1, p. e20039, 2022. https://doi.org/10.1002/ppj2.20039

[17] S. Wu *et al.*, “Extraction and mapping of cropland parcels in typical regions of southern China using unmanned aerial vehicle multispectral images and deep learning,” *Drones*, vol. 7, no. 5, p. 285, 2023. https://doi.org/10.3390/drones7050285

[18] M. Kumar, B. K. Bhattacharya, M. R. Pandya, and B. K. Handique, “Machine learning based plot level rice lodging assessment using multi-spectral UAV remote sensing,” *Computers and Electronics in Agriculture*, vol. 219, p. 108754, 2024. https://doi.org/10.1016/j.compag.2024.108754

[19] D. Zhang, X. Han, F. Lin, S. Du, G. Zhang, and Q. Hong, “Estimation of winter wheat LAI based on feature fusion of multi-source UAV imagery,” *Transactions of the Chinese Society of Agricultural Engineering*, vol. 38, no. 09, pp. 171–179, 2022. https://kns.cnki.net/kcms2/article/abstract?v=NitQnVYDOco--eBN-BExdTosW2DqRK-fD1lNEDvlC-A5RPvQTNnApY-cqgIhc2uz9q5LjvrqhvT0ngPI90km3E7mN4b1X3L_M_VicXx4XUp6VNKju3CchAF-btApx3Tr9HqfgImgxk0ABQyGMQscJdaA0An0lpJqkh2rNvjf7CoxHOqrZiQEKlonU39zDsaD7&uniplatform=NZKPT&language=CHS

[20] Y. Che *et al.*, “High-quality images and data augmentation based on inverse projection transformation significantly improve the estimation accuracy of biomass and leaf area index,” *Computers and Electronics in Agriculture*, vol. 212, p. 108144, 2023. https://doi.org/10.1016/j.compag.2023.108144

[21] X. Han, “Monitoring of winter wheat growth and yield estimation using multi-source UAV remote sensing imagery,” Master’s thesis, Anhui University, 2022. [Online]. Available: https://link.cnki.net/doi/10.26917/d.cnki.ganhu.2022.000416

[22] H. Fu *et al.*, “Screening method of high-quality ramie germplasm resources based on UAV remote sensing phenotypic monitoring,” *Smart Agriculture*, vol. 4, no. 4, pp. 74–83, 2022. [Online]. Available: https://link.cnki.net/urlid/10.1681.S.20221130.1200.001

[23] Y. Bai, “Research on remote sensing monitoring of maize seedling growth based on UAV multi-source imagery,” Master’s thesis, Chinese Academy of Agricultural Sciences, 2022. [Online]. Available: https://link.cnki.net/doi/10.27630/d.cnki.gznky.2022.000417

[24] L. Meng *et al.*, “Improved crop biomass algorithm with piecewise function (iCBA-PF) for maize using multi-source UAV data,” *Drones*, vol. 7, p. 254, 2023. https://doi.org/10.3390/drones7040254

[25] Z. Li *et al.*, “A hierarchical interannual wheat yield and grain protein prediction model using spectral vegetative indices and meteorological data,” *Field Crops Research*, vol. 248, p. 107711, 2020. https://doi.org/10.1016/j.fcr.2019.107711

[26] X. Han *et al.*, “A fully convolutional neural network model combined with a Hough transform to extract crop breeding field plots from UAV images,” *International Journal of Applied Earth Observation and Geoinformation*, vol. 132, p. 104057, 2024. https://doi.org/10.1016/j.jag.2024.104057

8 AUTHORS

Yibo Wei is with the Beijing Research Center for Information Technology in Agriculture, Beijing Academy of Agriculture and Forestry Sciences, Beijing, 100097, China.

Dong Cai is with the NongXin Science & Technology (Tianjin) Co., Ltd., Tianjin, 302602, China.

Haoyu Wang is with the Beijing Research Center for Information Technology in Agriculture, Beijing Academy of Agriculture and Forestry Sciences, Beijing, 100097, China.

Xinyi Wang is with the Beijing Research Center for Information Technology in Agriculture, Beijing Academy of Agriculture and Forestry Sciences, Beijing, 100097, China.

Xiaohong Du is with the Beijing Research Center for Information Technology in Agriculture, Beijing Academy of Agriculture and Forestry Sciences, Beijing, 100097, China.

Jiangchuan Fan is with the Beijing Research Center for Information Technology in Agriculture, Beijing Academy of Agriculture and Forestry Sciences, Beijing, 100097, China (E-mail: fanjc@nercita.org.cn).